The effect of dynamic recrystallization on olivine fabric and seismic anisotropy: Insights from a ductile shear zone in the Oman ophiolite

The effect of dynamic recrystallization on olivine fabric and seismic anisotropy: Insight from a ductile shear zone, Oman ophiolite

Katsuyoshi Michibayashi[a,*], Toshiki Ina[a], Kyuichi Kanagawa[b]

[a] Institute of Geosciences, Shizuoka University, Shizuoka 422-8529, Japan

[b] Department of Earth Sciences, Chiba University, Chiba, 263-8522, Japan

* corresponding author: sekmich@ipc.shizuoka.ac.jp, fax:+81-54-238-4788

Abstract

Subhorizontal mantle structures subparallel to the Moho are rotated into NW-SE subvertical orientations across a shear zone in a sinistral sense of shear within the northern Fizh mantle section of the Oman ophiolite. Dynamic recrystallization resulted in grain size reduction of olivine and the development of porphyroclastic texture. Mean olivine grain size stabilized at ~0.7 mm within the shear zone center; this may reflect the steady-state grain size of dynamically recrystallized olivine, as determined by the deviatoric stress, which in this case was as low as 10 MPa. Crystal-preferred orientation (CPO) patterns of olivine are consistently [100]-fiber or partial fiber texture, indicating that olivine slip systems did not change during shearing. Dynamic recrystallization causes a weakening of olivine fabric intensity toward the shear zone center, but this weakening is counterbalanced by CPO strengthening due to dislocation glide. This process resulted in an abrupt decrease in seismic anisotropy at the center of the shear zone, in contrast to a gradual decrease in olivine fabric intensity and mean grain size.

The seismic anisotropy patterns measured do not change in ways that would be significantly measurable by seismological observations. Despite the development of the shear zone, dispersion of both P- and S-waves in the shear zone may be of little effect with respect to the overall seismic anisotropy. This is not only because the shear zone occurs substantially in a narrow region, but because the seismic anisotropy is weaker in the shear zone than the high-T structure region. It suggests that a record of simple systematic seismic anisotropy observed in the upper mantle may indicate a simplified mantle flow structure, as localized structures may be obscured in the region of the observation.

Key words: ductile shear zone, Oman ophiolite, porphyroclastic texture, olivine crystal-preferred orientation, dynamic recrystallization, seismic anisotropy

1.Introduction

The role of seismic anisotropy in understanding the evolution of the upper mantle has become increasingly important. Seismic anisotropy in the upper mantle is commonly linked to crystal-preferred orientation (CPO), in particular olivine CPO, for determining the flow direction and shear plane from seismic observations [e.g., 1-13]. However, the relationship between seismic anisotropy and mineral CPO depends on many factors, such as deformation history, deformation mechanisms, and the existence of water or melt in the rock [e.g., 14-17]. Therefore, we must understand how olivine CPO develops and evolves with strain within particular deformation settings.

Analysis of naturally and experimentally deformed upper mantle rocks enables the measurement of CPO patterns that may develop during plastic deformation. It is generally accepted that high-strain deformation and recrystallization of minerals results in the intense preferred orientation of mineral crystallographic axes, as demonstrated by both experimental and theoretical studies. In nature, the development of the strongest preferred orientation in olivine occurs commonly within structures reflecting high to very high temperature flow conditions [1]. Grain sizes of such mantle rocks are dominantly coarsely granular, such that subsequent deformation would likely occur as grain size reduction associated with dynamic recrystallization at lower temperatures and higher stress conditions, in particular within the oceanic lithosphere [e.g., 18]. Yet the quantitative relationship between CPO intensity and strain that accompanies grain size reduction and dynamic recrystallization is poorly understood, as natural peridotites generally lack both strain markers and strain paths [19]. Experimental high-shear deformation of olivine aggregates produces a stable CPO and recrystallized microstructure consistent with observations of highly deformed natural peridotites [17]. However, there are substantial differences in sample size, grain size, temperature, and strain rate conditions between experimental and natural examples. The similarities and differences between experimental and natural samples should therefore be quantified to enable the scaling of the results of experimental rock deformation studies to deformation within the Earth.

In this paper, we present microstructural data from an uppermost mantle shear zone in the Oman ophiolite to demonstrate the changes that occur in the uppermost

mantle as asthenospheric material cools and strain begins to localize into kilometer-scale shear zones. While the grain size decreases markedly with increasing stress during shearing, the CPO remains similar to that produced by high temperature deformation. As a result, the seismic anisotropy patterns do not change in a manner that would be measurable by seismological observations. We will discuss the implications of our results for the interpretation of seismic anisotropy in terms of geodynamic models.

2. Geological setting and sample description

The northern Fizh block is located in the northern part of the Oman ophiolite (Fig. 1), and many studies have been conducted in this area [20-26]. The Moho dips southeast at 10-40° at Wadi Zabin and in the southern portion of Wadi Rajmi, whereas it dips east at 30-80° in the northern portion of Wadi Rajmi [22]. The Fizh block is characterized by shear zones that strike NW-SE that penetrate both the mantle and the lowermost crustal section [16-20]. The shear zones are subvertical in the mantle section, and their foliations crosscut high-temperature mantle structures [22]. The Moho within the Fizh block is offset by a NW-SE striking sinistral shear zone. The shear zone cuts through a coarse granular domain with well-developed mylonitic texture, which grades over a lateral distance of 5 km along the shear zone into a porphyroclastic domain [26]. To the southeast, the shear zone can be traced up through the Moho into the crustal sequence where layered gabbro has been metamorphosed to amphibolite within a 10 m wide ductile shear zone [22, 25]. The samples analyzed in this study were collected from Wadi Rajmi in the northern Fizh mantle section, which consists dominantly of hartzburgite with porphyroclastic texture (Figs. 1 and 2) [26]. We measured foliation and lineation defined by the alignment of spinel grains in the field and checked field measurements on bleached and saw-cut samples in the laboratory. These structures are divided into two types: high-T and low-T types, based on microstructural criteria.

The orientations of lineations and foliations are shown in Fig. 2. High-T deformation is dominantly characterized by shallow dipping foliation planes and a NE-SW lineation. Lineations associated with high-T deformation at the margin of the shear zone have a N-S trend and are continuous with the low-T lineations. The trend of low-T lineations is progressively rotated sinistrally within shear zone; at the center of the

shear zone the lineation is parallel to the strike of the shear zone. Here, we define the center of the shear zone based on the field observation, where intense foliation and lineation are oriented subparallel to the strike of the macroscopic shear zone (Fig. 2). We also recognized a narrow zone of low-T deformation parallel to the Moho, where the foliation dips steeply and the lineation trend is subparallel to the Moho (Fig. 2).

3.Microstructural analysis

3.1. Microstructure

We analyzed microstructures in all samples using thin sections cut perpendicular to the foliation and parallel to the lineation (i.e. XZ-section). We analyzed in detail eight peridotite samples from across the shear zone (Fig. 2c). Peridotites were sampled from high-T deformation zones at the western margin to the eastern margin through the shear zone (A-H in Fig. 2c). The microstructure of these peridotites is shown in Fig. 3. The high-T samples are characterized by coarse granular texture consisting dominantly of coarse olivine grains (A and H in Fig. 3), whereas the low-T samples have variable microstructure in terms of grain size possibly related to variable strain along the shear zone (B-G in Fig. 3). The two peridotite samples from the margins of the shear zone contain coarse olivine grains with minor neoblasts (B and G in Fig. 3). Coarse olivine grains have intense undulose extinction and irregular grain boundaries; we call this medium-grained granular texture (Fig. 2c). The peridotite samples within the shear zone have porphyroclastic textures (Fig. 2c), in which pyroxene porphyroclasts occur within a matrix of fine-grained olivine neoblasts that exhibit varying degrees of recrystallization (C-F in Fig. 3). The shapes of neoblasts vary, but tend to be elongated.

3.2. Mean grain size of olivine

The effects of serpentinization make it difficult to measure grain sizes in the samples. We were only able to measure the mean grain size of olivine in each sample by the linear intercept method [27]. We counted the number of grain boundaries along the lineation (Dx) and normal to the foliation (Dz) using the optical microscope. We then estimated the mean grain size of olivine (D) from $D=\sqrt{Dx \cdot Dz}$ (Table 1 and Fig. 4). Although the average size of Dx is different from that of Dz due to the elongate shapes of

grains, the mean grain size, D, decreases from 1.7 mm at the western margin to a stable minimum of ~0.7 mm in the center of the shear zone. The grain size increases again to 1.4 mm toward the eastern margin.

Crystal-preferred orientation (CPO) of olivine

4.1. Methods

Olivine CPO was measured from highly polished XZ thin section using a JEOL 5600 SEM equipped with electron back scattered diffraction (EBSD) at Chiba University, Japan. To obtain a representative CPO of the rock, at least 100 to 150 grains for each phase need to be measured [e.g. 28]. We measured 183-291 olivine crystal orientations per sample, and the computerized indexation of the diffraction pattern was visually checked for each orientation (Fig. 5).

To characterize the CPO, we determined the fabric strength and the distribution density of the principal crystallographic axes [e.g. 4, 18]. The rotation matrix between crystal and sample co-ordinates is used to describe the orientation **g** of a crystal in sample co-ordinates. In practice, it is convenient to describe the rotation by a triplet of Euler angles, for example $\mathbf{g} = (\varphi_1, \phi, \varphi_2)$ used by Bunge [29]. The orientation distribution function (ODF), $f(\mathbf{g})$, is defined as the volume fraction of orientations with an orientation in the interval between **g** and **g**+d**g** in a space containing all possible orientations given by

$$\Delta V/V = \int f(\mathbf{g})\, d\mathbf{g}$$

where $\Delta V/V$ is the volume fraction of crystals with orientation **g**, $f(\mathbf{g})$ is the texture function and $d\mathbf{g} = 1/8\pi^2 \sin\phi d\varphi_1 d\phi d\varphi_2$ is the volume of the region of integration in orientation space. To quantify the degree of CPO, Mainprice and Silver [2] used the *J*-index, which is defined as:

$$J = \int f(\mathbf{g})^2\, d\mathbf{g}$$

The *J*-index has a value of 1 for a random distribution and a value of infinity for a single crystal. The *J*-index for olivine in our calculations has a maximum of ~250 because of the truncation of the spherical harmonic series at an expansion of 22.

In a similar manner, the sharpness of a pole figure can be analytically defined by the *pfJ* index as:

$$pfJ = \int P_{hkl}(\alpha,\beta)^2 \, d\omega$$

where α and β are the spherical co-ordinates of the considered direction in the pole figure, $P_{hkl}(\alpha, \beta)$ is the density in that direction for a given crystallographic pole defined by hkl and $d\omega=1/2\pi\sin\alpha d\alpha d\beta$ is the volume of the region of integration. The *pfJ* index has a value of 1 for a random distribution and a maximum value for olivine of about 60 in the present case (which depends on the crystal symmetry and the symmetry of the crystal direction) for a single crystal of olivine. In the present case of olivine, the [100], [010] and [001] axes are all two-fold rotation axes; the *pfJ* values can therefore be directly compared.

4.2. Olivine CPO patterns

The measured olivine CPO is presented on equal area, lower hemisphere projections in the structural (XZ) reference frame (Fig. 5). Two samples with coarse granular textures show [100]-fiber CPO patterns, which are characterized by a strong alignment of [100] close to the lineation and by a distribution of [010] and [001] in a girdle normal to the [100] maximum (A and H in Fig. 5). However, alignment of [010] and [001] is different between the two samples. Sample 01OK60 has a weak bimodal alignment of [010] with a single concentration of [001] parallel to the Y-axis (Fig. 5A), whereas sample 01OK71 contains alignments of both [010] and [001] parallel to the pole to the foliation with only weak alignment parallel to the Y-axis (Fig. 5H). Two samples with medium-grained granular textures (Fig. 5B and G) are characterized by a strong alignment of [100] close to the lineation and by a distribution of [010] and [001] in a

girdle normal to the [100] maximum, with a weak bimodal alignment. These patterns are similar to the partial fiber texture described by Bunge [29], which has axial symmetry with the [100] as a rotational axis of symmetry, and [010] and [001] forming girdles in the YZ structural plane normal to the lineation; this type can have maxima of [010] and [001] parallel to either of the Y or Z directions [22].

In the center of the shear zone, sample 01OK66 has an orthorhombic CPO pattern, which is characterized by a strong alignment of [100] close to the lineation, alignment of [010] perpendicular to the lineation on the foliation plane, and alignment of [001] normal to the foliation (Fig. 5C). Among the three axes, [010] has the weakest concentration. The other three samples show weaker CPO patterns (D-F in Fig. 5), characterized by an alignment of [100] close to the lineation and by a distribution of [010] and [001] in a girdle approximately normal to the [100] maximum. In addition, the two samples 01OK67 (Fig. 5D) and 01OK68 (Fig. 5E) show similar features of CPO patterns to the sample 01OK60 (Fig. 5A), whereas the sample 01OK69 (Fig. 5F) has similar CPO patterns to the sample 01OK66 (Fig. 5C).

4.3. Intensity of olivine CPO

The degree of fabric intensity for all samples is shown in Table 2 and Figs. 4 and 5. The *J*-index decreases from 11 at the western margin to as low as 4.2 in the center of the shear zone, and increase again to 10.1 at the eastern margin (Fig. 4a). High values of *J*-index are associated with high-T samples (A and H). Within the shear zone, the *J*-index appears to be stable at around 4.3 (D-F). The trends of the pole figure index *pfJ* generally follow the trends of the *J*-index. The [100] pole figure index has the highest intensity of the three axes for all samples.

5. Seismic properties

5.1. Methods

The seismic properties of a rock mass can be computed by averaging the elastic constants of the individual grains in all directions, taking into account the crystallographic orientation of the main mineral phases and the modal composition of the aggregate [4, 30]. In this study, it is difficult to determine the modal composition of

minerals in the samples because of serpentinization. Therefore, we calculated the seismic properties by assuming a composition of 100% olivine, which is the volumetrically dominant phase in the samples. The effect of additional phases (e.g., orthopyroxene) will be to reduce the overall seismic anisotropy but does not change the anisotropy patterns [e.g., 2, 31]. The elastic constants of olivine used for the calculations are from Abramson et al. [32], at ambient conditions. The derivatives of elastic stiffness on both temperature and pressure are linear, so that the P-T conditions affect the velocity values, but leave the anisotropy unchanged [28]. We used the Voigt Reuss Hill averaging scheme [4]. The anisotropy of P-waves is defined as a percentage by the formula $200(Vp_{max} - Vp_{min})(Vp_{max} + Vp_{min})$, while the anisotropy of S-waves (AVs) is defined for a specific propagation direction by the formula $200(Vs_1-Vs_2)/(Vs_1+Vs_2)$, where Vs_1 and Vs_2 are the fast and slow wave velocities, respectively [2].

5.2. Results

The P-wave is fastest subparallel to lineation, which is closely related to the CPO maximum of olivine [100] (Fig. 5), the fast direction within olivine crystals (Fig. 6). The P-wave is low for waves propagating in a plane normal to the [100] maximum, resulting in an axial symmetry with the [100] maximum as the symmetry axis (Fig. 6). Polarization anisotropies of most samples have two maxima girdles on each side of a plane normal to the [100] maximum, whereas the minimum birefringence occurs for propagation directions close to the [100] maximum subparallel to the lineation (Fig. 6). The orientation of the polarization plane of the fastest S-wave systematically marks the orientation of the great circle containing the maximum concentration of [100] (Fig. 6).

A systematic trend in seismic anisotropy is apparent across the shear zone (Fig. 4b). The P-wave anisotropy decreases from 11.9 % at the western margin to 8.3 % in the shear zone center and increases again to 13.3 % at the eastern margin (Fig. 4b). The decrease in P-wave anisotropy is consistent with a decrease of P-wave maximum velocity; P-wave minimum velocity remains largely unchanged across the shear zone (Fig. 4b). S-wave polarization anisotropy decreases from 8.25 % at the western margin to 5.29 % in the shear zone center and increases again to 9.27 % at the eastern margin (Fig. 4b). This trend is similar to that for P-wave anisotropy (Fig. 4b).

6. Interpretation and Discussion

6.1. CPO intensity vs. grain size reduction with finite strain

Whereas microstructure changes from coarse granular texture at the margin of the shear zone to porphyroclastic texture in the center (Fig. 2c), mean grain size decreases toward the center of the shear zone and appears to stabilize at around 0.7 mm size within the center of the shear zone (Fig. 4a and Table 1). This decrease is due to dynamic recrystallization resulting in porphyroclastic texture. Grain size is expected to change until recrystallized grains attain the steady-state grain size, which is determined by the deviatric stress [33]. If we assume that the stable mean grain size in the shear zone is a steady-state grain size, we can then use grain size as a paleopiezometer to infer flow stress [e.g. 33, 34]. Figure 7 shows the relationship between grain size and differential stress (after Jung and Karato [35]), where the steady-state grain size estimated for the rocks analyzed in this study is indicated by the arrow. Although the mean grain size in this section of the shear zone is too coarse to compare with experimental results, the development of porphyroclastic texture from coarse granular texture probably requires only a very small deviatric stress, possibly as low as 10 MPa (Fig. 7), which is for example compatible with those estimated for the coarse Othris peridotite tectonites [36].

Experimental high-shear deformation of olivine aggregates produces a stable CPO and recrystallized microstructure [17] that yields remarkably similar microstructures and CPO to the shear zone analyzed in this study. Whereas we show a microstructural transition from high-temperature coarse granular texture to lower-temperature porphyroclastic texture (Figs. 2 & 3) with CPO patterns that are consistently [100]-fibre or partial fiber texture across the shear zone (Fig. 5), the experimental study shows essentially the same microstructure as the high strain shear zone fabrics [17]. It is interesting to note that the variation in olivine fabric intensity with respect to strain in the natural samples is opposite that in the experimental samples. Figure 4a shows that the olivine fabric decreases in intensity toward the shear zone center, whereas the CPO strength increases with strain in the experiments [17]. This trend is mainly due to the fabric intensity of the primary olivine microstructure, as indicated by

the *J*-index values, which are 11 and 9.1, respectively, at the margin of the shear zone (Fig. 4a and Table 2), and 1.4 at a shear strain of ~0.5 in the experiments [17].

Recrystallized grains display a clear misorientation relative to the parent grains [19]. Dynamic recrystallization via nucleation and growth of strain-free neoblasts at grain boundaries [37] may also result in an effective weakening of the CPO [12, 38]. We therefore consider that the primary CPO in samples with coarse granular texture is weakened as a consequence of intense dynamic recrystallization. However, the olivine fabric intensity appears to be stable in the shear zone center (Fig. 4a). Tommasi et al. [19] suggested that dynamic recrystallization by subgrain rotation stabilizes the CPO. Subgrain rotation is characterized by subdivision of strained porphyroclasts into new grains displaying a misorientation of >15° relative to the parent grain [39]. This may induce a progressive weakening of CPO that is countered by CPO intensification resulting from dislocation glide, giving rise to a stable CPO (see [19]).

Porphyroclastic texture is a mixture of coarse porphyroclasts and dynamically recrystallized neoblasts and therefore it has a wide range of microstructures that are dependent on the rate of dynamic recrystallization. It is likely that as grain size reduction progressed toward a steady-state grain size, the proportion of neoblasts increased and the average grain size decreased. In this case, although it is difficult to recognize a recrystallization mechanism within our samples because of intense serpentinization, dynamic recrystallization by subgrain rotation could result in a weakening of the CPO. If we assume a strain gradient from the center to the margin of the shear zone in Fig. 4a, it indicates that the amount of strain required to develop a steady-state grain size is lower than that for stabilizing fabric intensity.

6.2. CPO pattern evolution

Both foliation and lineation orientations indicate that olivine CPO patterns were gradually rotated from the primary subhorizontal NE-SW flow direction to a secondary subvertical NW-SE flow direction (Figs. 2 and 4). This rotation of the structural framework is similar to a shear zone documented in the Hilti mantle section, located to the south of the Fizh mantle section, documented by Michibayashi and Mainprice [18]. They demonstrated that although the dominant slip system varies from

(010)[100] in high-T deformation to (001)[100] in low-T deformation, the [010]-axis remains geographically vertical in both cases. Rotation about the [010]-axis appears to lead to (001)[100] slip, and sinistral slip of the shear zone developed sub-vertically without changing the CPO orientation. In the present study, although both foliation and lineation orientations indicate that olivine CPO patterns were gradually rotated from the primary subhorizontal NE-SW flow direction to the secondary subvertical NW-SE flow direction (Figs. 2 and 5), CPO patterns remain largely unchanged from the margin to the center of the shear zone.

[100]-fiber CPO patterns are dominant across the shear zone (Fig. 5), indicating that the {0kl}[100] slip system is active for these CPO patterns at medium temperature conditions such as 1000 °C (e.g. [1]). In more detail, the CPO patterns vary, as the fabric intensity is weakened toward the shear zone center as discussed above. At the shear zone margins, samples A and H in Fig. 5 have coarse granular texture and show {0kl}[100] patterns with bimodal maxima in both [010] and [001] to Y-axis and Z-axis. This pattern may be preserved within transitional texture such as B and G in Fig. 5, as these foliations and lineations were rotated while accompanied by only weak grain size reduction (Fig. 4a). As the fabric intensities are weak, CPO patterns vary within the shear zone. C and F show a (001)[100] pattern, whereas D and E are dominated by a (010)[100] pattern (Fig. 5). These trends can be explained by selective recrystallization of those grains in hard orientations. Grains in hard orientations (e.g., those with [100] parallel to σ_1) suffer intense kinking [8] and therefore act as preferential sites for recrystallization [19]. CPO maxima could therefore be inherited from those parts of the earlier CPO that did not undergo recrystallization: those of 'easy' rather than hard slip systems [18]. Alternatively, Tommasi et al. [19] suggested that during simple shear, recrystallization by either subgrain rotation or grain boundary migration leads to a single maxima CPO in which the main slip system is parallel to macroscopic shear. In either case, the main slip systems for the two CPO patterns documented in the shear zone could well be (001)[100] and (010)[100]. In this case, both slip systems would be equally active in developing porphyroclastic texture within the shear zone.

As the (010)[100] slip system is active at high-temperatures, the difference between the results of this study and those of Michibayashi and Mainprice [18] may be

explained by the effect of temperature on dynamic recrystallization. The cross-section analyzed in this study is located within the zone of only porphyroclastic texture within the northern Fizh shear zone, whereas Michibayashi and Mainprice [18] studied the zone within the Hilti shear zone where mylonite and ultramylonite also occurred in addition to porphyroclastic texture. It suggests that the Hilti shear zone developed under lower temperatures or higher stress than the northern Fizh shear zone.

6.3. Influence of CPO intensity and CPO patterns on seismic properties

Ben Ismaïl and Mainprice [28] showed that the seismic properties of a rock, as a function of fabric strength, display an exponential relationship between the *J*-index and seismic anisotropy of both P-waves and S-waves. Figure 8 displays an exponential relationship similar to that of Ben Ismaïl and Mainprice [28]. Mainprice and Silver [2] used the experimental data of Nicolas et al. [12] to show that the *J*-index increases with increasing axial strain; Ben Ismaïl and Mainprice [28] therefore use the *J*-index as an indicator of plastic strain to a first approximation [cf. 19]. In the present study, it is more likely that a series of samples across the shear zone could display a strain gradient from the margin to the center (Fig. 2). Figure 4b shows that the *J*-index does not strictly correlate with the seismic anisotropy of both P- and S-waves from the margin to the center of the shear zone. Instead, the seismic anisotropies decrease rather abruptly near the shear zone center (Fig. 4b), at the point where both mean grain size and fabric intensity are stabilized (Fig. 4a). Figure 4b also demonstrates that the decrease in seismic anisotropy of P-waves results from a decrease in maximum P-wave velocity, while almost no change occurs in terms of minimum P-wave velocity. A similar trend can be seen in S-wave data (Table 2). Ben Ismaïl and Mainprice [28] suggested that increasing alignment of the [100] axes induces an increase in P-wave seismic anisotropy, whereas the orientation of the [010] and [001] axes have only a secondary effect. Indeed, *pfJ* of the [100] axis for samples with lower seismic anisotropies (D, E, F and G) decreased to less than 3, suggesting that the P-wave seismic anisotropy decreases with decreasing alignment of the [100] axes. A similar trend can be observed for S-wave seismic anisotropy, as all three axes influence the magnitude of S-wave anisotropy [28]. As a consequence, dispersion of the three axes due to dynamic recrystallization associated

with low-temperature strain and higher deviatoric stress has influenced the seismic anisotropy of both P- and S-waves.

6.5. Implication for the interpretation of seismic anisotropy in the mantle lithosphere

Although a textural transition occurs from coarse granular to porphyroclastic texture across the shear zone, CPO patterns are mostly [100]-fiber or partial fiber textures. This consistency of CPO patterns results in similar seismic properties for all samples across the shear zone (Fig. 6). It is important to note that the orientation of the structural framework changes over space from subhorizontal N-S flow to subvertical NW-SE flow (Figs. 2 and 4). A certain amount of change in seismic anisotropy could therefore result from the orientation of the structural framework despite the similarity in seismic properties across the shear zone. However, we argue that the overall seismic anisotropy may be not influenced by the orientation of the structural framework. This is not only because the shear zone occurs substantially in a narrow region, but because the seismic anisotropy is weaker in the shear zone than in the high-T structure region. Dispersion of both P- and S-waves in the shear zone may therefore be of little effect with respect to the overall seismic anisotropy. Seismic anisotropy analysis is therefore unable to locate such a shear zone in the upper mantle unless the resolution is as fine as one kilometer.

Our results may help to understand at which stage the anisotropy develops during formation of the plate, and what aspects of plate formation processes control the seismic properties of the plate. Our results indicate that the anisotropy forms quite early, when the rocks were still close to the ridge [e.g., 40, 41]. Subsequently, the anisotropy will not be altered, even if the plate is deformed under different kinematic constraints such as localized deformation within a shear zone. Consequently, the ‘anisotropy memory’ of a plate is long, as the imprint of ridge processes are very strong and it is difficult to erase them. In subduction zones, high shear strains may lead to strain localization where hot mantle convects past the upper side of cold subducting slabs, whereas strain weakening may focus on major detachment zones near the crust-mantle boundary in regions of extensional deformation [17]. However, these tectonic events might remain undetected by seismic anisotropy observations, unless significant features of the events appear on the surface [e.g., 42, 43].

7. Conclusions

Our (micro-)structural and petrophysical study of the northern Fizh shear zone in the Oman ophiolite demonstrates the changes that occur in the uppermost mantle as asthenospheric material cools and strain is localized into a kilometer-scale shear zone.

Dynamic recrystallization resulted in grain size reduction of olivine and the development of porphyroclastic texture. Mean olivine grain size stabilized at ~0.7 mm within the shear zone center, which may reflect the steady-state grain size of dynamically recrystallized olivine; this is determined by the deviatoric stress, which could be as low as 10 MPa.

Crystal-preferred orientation (CPO) patterns of olivine are consistently [100]-fiber or partial fiber texture, indicating that olivine slip systems did not change during shearing. Dynamic recrystallization causes a weakening of olivine fabric intensity toward the shear zone center, but this weakening is counterbalanced by CPO strengthening due to dislocation glide. This process resulted in an abrupt decrease in seismic anisotropy at the center of the shear zone, in contrast to gradual decreases in olivine fabric intensity and mean grain size.

The microstructural transition from high-temperature coarse granular to lower-temperature porphyroclastic textures across the shear zone is compatible with textures produced by the experimental high shear deformation of olivine aggregates. However, the relationship between olivine fabric intensity and strain is opposite in the naturally and experimentally deformed samples, possibly due to differences in primary fabric intensity.

The seismic anisotropy patterns measured in this study do not change in ways that would be significantly measurable by seismological observations. Despite the development of the shear zone, dispersion of both P- and S-waves in the shear zone will be of little effect with respect to the overall seismic anisotropy.

ACKNOWLEDGEMENTS

Drawings of CPO and calculations of seismic anisotropy were performed using the interactive programs of David Mainprice of Université Montpellier II, France. Aaron

Stallard, David Jousselin, and an anonymous reviewer provided valuable suggestions that helped to improve the paper. The authors thank Aaron Stallard, University of Canterbury, New Zealand, for improving the English of the manuscript. We would like to thank Sumio Miyashita, Shoji Arai, Toshiaki Masuda and Susumu Umino for their leaderships in our field study to the Oman ophiolite from 1999 to 2001. We greatly thank to Hilal Al Azri, the Deputy Director General of Minerals, Ministry of Commerce and Industry of Oman as a sponsor of our field study. We also thank to Eiichi Takazawa, Tsutomu Sato, Tsuyoshi Ishikawa, Yoshiko Adachi, Norihiro Odashima, Adolphe Nicolas, François Boudier, Benoit Ildefonse and David Mainprice for their support during this study. This work was financially supported by research grants from the Japan Society of the Promotion of Science and Ministry of Education, Culture, Sports, Science and Technology of Japan.

REFERENCES

[1] Nicolas, A. & Christensen, N. I. (1987). Formation of anisotropy in upper mantle peridotite: A review, in Composition Structure and Dynamics of the Lithosphere-Asthenosphere System, Geodyn. Monogr. Ser., In: Fuchs, K. & Froidevaux, C. (eds) pp. 111-123, AGU, Washington, D. C.

[2] Mainprice, D. & Silver, P. G. (1993). Interpretation of SKS-waves using samples from the subcontinental lithosphere. Physics of Earth and Planetary Interior 78, 257-280.

[3] Vauchez, A., Barruol, G & Tommasi, A. (1997) Why do continents split parallel to ancient orogenic belts? Terra Nova, 9, 62-66.

[4] Mainprice, D., Barruol, G. & Ben Ismaïl, W. (2000). The anisotropy of the Earth's mantle: From single crystal to polycrystal. In: Karato, S., Forte, A.M., Liebermann, R.C., Masters, G. & Stixrude, L. (eds) Mineral Physics and Seismic Tomography: From Atomic to Global, AGU Geophysical Monograph 117, pp. 237-264.

[5] Blackman, D. K., Wenk, H. –R. & Kendall, J. –M. (2002) Seismic anisotropy in the upper mantle 1. Factors that affect mineral texture and effective elastic properties, Geochem. Geophys. Geosyst., 3(9), 8601, doi: 10.1029/2001GC000248.

[6] Hammond, W. C. & Toomey, D. R. (2003) Seismic velocity anisotropy and heterogeneity beneath the Mantle Electromagnetic and Tomography Experiment (MELT) region of the East Pacific Rise from analysis of *P* and *S* body waves. J. Geophys. Res. 108, 2176, doi: 10.1029/2002JB001789.

[7] Karato, S. & Wu, P. (1993) Rheology of the upper mantle: a synthesis. Science, 260, 771-778.

[8] Nakajima, J. and Hasegawa, A. (2004) Shear-wave polarization anisotropy and subduction-induced flow in the mantle wedge of northeastern Japan. Earth Planet. Sci. Lett. 225, 365-377.

[9] Ishise, M. and Oda, H. (2005) Three-dimensional structure of P-wave anisotropy beneath the Tohoku district, northeast Japan. J. Geophys. Res. 110, B07304, doi:10.1029/2004JB003599.

[10] Birch, F. (1961) The velocity of compressional waves in rocks to 10 kbar, Part 2. J. Geophys. Res. 66, 2199-2224.

[11] Babuska, V. (1972) Elasticity and anisotropy of dunite and bronzitite. J. Geophys. Res. 77, 6955-6965.

[12] Nicolas, A., Boudier, F. & Boullier, A. M. (1973). Mechanism of flow in naturally and experimentally deformed peridotites. American Journal of Science 273, 853-876.

[13] Christensen, N. I. and Lundquist, S. M. (1982) Pyroxene orientation within the upper mantle. Geol. Soc. Am. Bull. 93, 279-288.

[14] Jung, H. and Karato, S. (2001) Water-induced fabric transitions in olivine, Science, 1460-1463.

[15] Holtzman, B. K., Kohlstedt, D. L., Zimmerman, M. E., Heidelbach, F., Hiraga, T. and Hustoft, J. (2004) Melt segregation and strain partitioning: implications for seismic anisotropy and mantle flow, Science, 1227-1230.

[16] Katayama, I., Jung, H. and Karato, S. (2004) New type of olivine fabric from deformation experiments at modest water content and low stress, Geology, 32, 1045-1048.

[17] Bystricky, M., Kunze, K., Burlini, L. & Burg, J. –P. (2000) High shear strain of olivine aggregates: rheological and seismic consequences, Nature, 290, 1564-1567.

[18] Michibayashi, K. & Mainprice, D. (2004). The role of pre-existing mechanical anisotropy on shear zone development within oceanic mantle lithosphere: an example from the Oman ophiolite. Journal of Petrology, 45, 405-414.

[19] Tommasi, A., Mainprice, D., Canova, G. & Chastel, Y. (2000). Viscoplastic self-consistent and equilibrium-based modeling of olivine lattice preferred orientations. Implications for upper mantle seismic anisotropy. Journal of Geophysical Research 105, 7893-7908.

[20] Smewing, J. D. (1980) An uppere Cretaceous ridge-transform intersection in the Oman ophiolite, in Ophiolites, Proceedings of the International Ophiolite Symposium, Cyprus, 1979, edited by A. Panayiotou, pp. 407-413, Geol. Surv. Dep., Minist. Agric. and Nat. Resour., Cyprus.

[21] Lippard, S. J., Shelton, A. W. and Gass, I. G. (1986) The ophiolite of northern Oman, in The Geological Society Memoirs, vol. 11, 178 pp., Blackwell Sci., Malden, Mass.

[22] Boudier, F., Ceuleneer, G. & Nicolas, A. (1988). Shear zones, thrusts and related magmatism in the Oman ophiolite: initiation of thrusting on an oceanic ridge. Tectonophysics 151, 275-296.

[23] Nicolas, A., Ceuleneer, G., Boudier, F. and Misseri, M. (1988) Structural mapping in the Oman ophiolites: Mantle diapirism along an oceanic ridge, Tectonophysics, 151, 27-56.

[24] Reuber, I. (1988) Complexity of the crustal sequence in the northern Oman ophiolite (Fizh and southern Aswad blocks): The effect of early slicing? Tetonophysics, 151, 137-165,

[25] Nicolas, A., Boudier, F., Ildefonse, B. & Ball, E. (2000). Accretion of Oman and United Arab Emirates ophiolite – Discussion of a new structural map. Marine Geophysical Researches 21, 147-179.

[26] Takazawa, E., Okayasu, T. and Satoh, K. (2003) Geochemistry and origin of the basal lherzolites from the northern Oman ophiolite (northern Fizh block), Geochemistry Geophysics Geosystems, 4, 1021, doi:10.1029/2001GC000232.

[27] Smith, C. S. and Guttman, L. (1953). Measurement of internal boundaries in three-dimensional structures by random sectioning. Trans. Am. Inst. Min. Eng. J. Metals, 197, 81-87.

[28] Ben Ismaïl, W. & Mainprice, D. (1998). An olivine fabric database: an overview of upper mantle fabrics and seismic anisotropy. Tectonophysics 296, 145 - 157.

[29] Bunge, H. J. (1982). Texture Analysis in Materials Sciences, 593 pp., Butterworths, London.

[30] Mainprice, D. & Humbert, M. (1994) Methods of calculating petrophysical properties from lattice preferred orientation data. Surv. Geophys. 15, 575–592.

[31] Barruol, G. and Mainprice, D. (1993) A quantitative evalution of the contribution of crustal rocks to shear-wave splitting of teleseismic SKS-waves. Phys. Earth Planet. Inter. 78, 2881-300.

[32] Abramson. E. H., Brown, J. M., Slutsky, L. J. and Zang, J. (1997) The elastic constants of San Carlos olivine to 17 GPa. J. Geophys. Res., 102 (6), 12253-12263.

[33] Twiss, R. J., 1977. Theory and applicability of a recrystallized grain size paleopiezometer. Pure. Appl. Geophys., 115, 227-244.

[34] Michibayashi, K. (1993) Syntectonic development of a strain independent dynamically recrystallized quartz grain during mylonitization. Tectonophysics, 222, 151-164.

[35] Jung, H. and Karato, S. –H. (2001) Effects of water on dynamically recrystallized grain size of olivine. J. Struct. Geol. 23, 1337-1344.

[36] Dijkstra, A. H., Drury, M. R., Vissers, R. L. M. & Newman, J. (2002) On the role of melt-rock reaction in mantle shear zone formation in the Othris Peridotite Massif (Greece). J. Struct. Geol. 24, 1431-1450.

[37] Drury, M. R., Vissers, R. L. M., van der Wal, D. and Strating, E. H. H. (1991) Shear localisation in upper mantle peridotites. Pure Appl. Geophys. 137, 439-460.

[38] Boudier, F. and Coleman, R. G. (1981) Cross section through the peridotites in the Samail ophiolite, southeastern Oman mountain. J. Geophys. Res. 86, 2573-2592.

[39] Poirier, J. P. & Nicolas, A. (1975). Deformation-induced recrystallization due to progressive misorientation of subgrains, with special reference to mantle peridotites, J. Geol. 83, 707-720.

[40] Ildefonse, B., Billiau, S. and Nicolas, A., 1995, A detailed study of mantle flow away from diapirs in the Oman ophiolite. In R.L.M. Vissers and A. Nicolas (eds), *Mantle*

and Lower Crust Exposed in Oceanic Ridges and in Ophiolites, Kluwer Academic Publishers, Dordrecht, pp. 163–177.

[41] Michibayashi, K., Gerbert-Gaillard, L. & Nicolas, A. (2000) Shear sense inversion in the Hilti mantle section (Oman ophiolite) and active mantle uprise. Marine Geophysical Researches, 21, 259-268.

[42] Tommasi, A. & Vauchez, A. (2001) Continental rifting parallel to ancient collisional belts: an effect of the mechanical anisotropy of the lithospheric mantle. Earth Planet. Sci. Lett. 185, 199-210.

[43] Heintz, M., Vauchez, A., Auumpção, M., Barruol, G. & Egydio-Silva, M. (2003) Shear wave splitting in SE Brazil: an effect of active or fossil upper mantle flow, or both? Earth Planet. Sci. Lett. 211, 79-95.

Figure captions

Figure 1. Locality map and generalized geology of the northern part of the Oman ophiolite. The locality of Figure 2 is shown by the box, where a ductile shear zone with a sinistral sense of shear crosscuts high-T structure.

Figure 2. Structural data from Wadi Rajmi. (a) Planar structures. The width of the shear zone is based on field observations. (b) Lineation structures. The dominant trend of the high-T lineations close to the Moho is NE-SW, whereas the N-S trend of high-T lineations is gradually rotated to NW-SE trend in low-T lineations, via a sinistral sense of shear. (c) Microstructural classifications along Wadi Rajmi. Each label is used in subsequent figures.

Figure 3. Photomicrographs of peridotite samples. The labels are the same as those in Fig. 2.

Figure 4. (a) Fabric intensity and grain size with respect to distance across the shear zone. Structural data are shown below the diagram. The center and margin zones are defined based on fabric intensity and grain size data. The text 'Field observation' indicates the width of the shear zone identified in the field. (b) Anisotropy of both P-wave (Vp) and S-wave (Vs) and maximum and minimum P-wave velocity with respect to distance across the shear zone.

Figure 5. Olivine CPO within analyzed samples. Equal area projection, lower hemisphere. Contours are in multiples of uniform distribution (m.u.d.). Foliation is vertical (XY plane; solid line) and lineation (X) is horizontal within the plane of the foliation. The labels are the same as those in Fig. 2.

Figure 6. Seismic anisotropy of olivine within analyzed samples. Equal area projection, lower hemisphere. Contours in m.u.d. Contours for Vp are in km/s, dVs in % anisotropy and trace of the Vs1 polarization plane. Foliation is vertical (XY plane; solid line) and lineation (X) is horizontal within the plane of the foliation. The labels are the same as those in Fig. 2.

Figure 7. Relationships between differential stress and recrystallized grain size (after Jung and Karato, 2001). The arrow indicates the mean grain size estimated from the shear zone center.

Figure 8. Relationships between seismic anisotropy and fabric strength (*J*-index) for Vp and Vs anisotropy. The labels are the same as those in Fig. 2. Gray solid and broken lines are the best fit of exponential curves. See text for discussion.

Table 1. List of samples and grain size data.

Table 2. Olivine fabric intensity and seismic properties for Vp and Vs.

Figure

Click here to download Figure: Fig 1-index map.eps

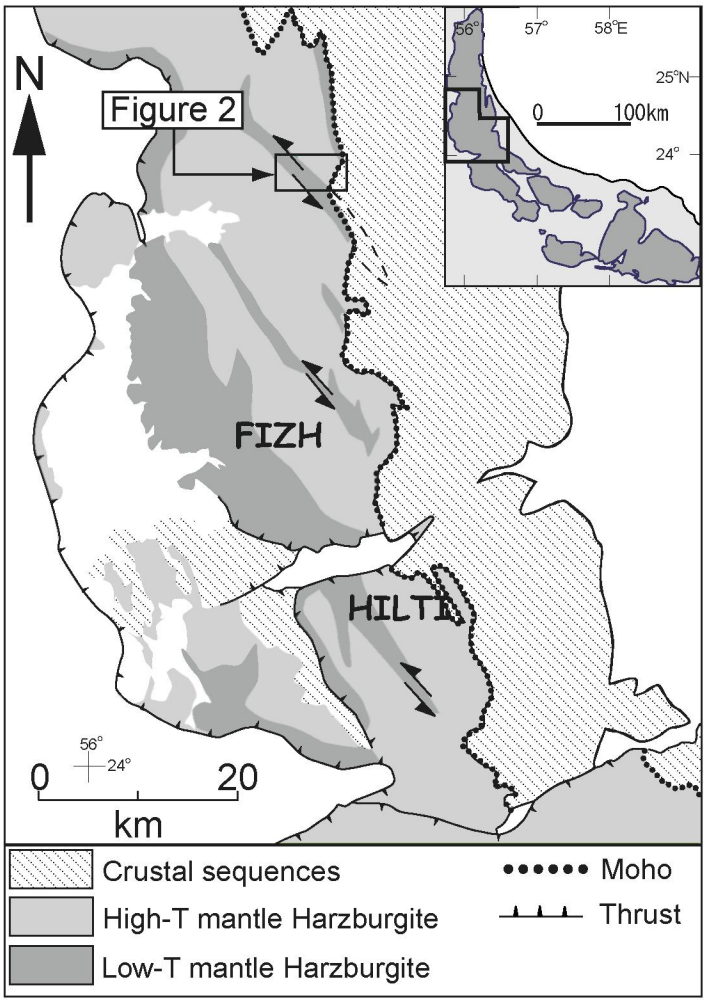

Fig. 1: Michibayashi, Ina and Kanagawa

Figure

Click here to download Figure: Fig 2-SLmaps.eps

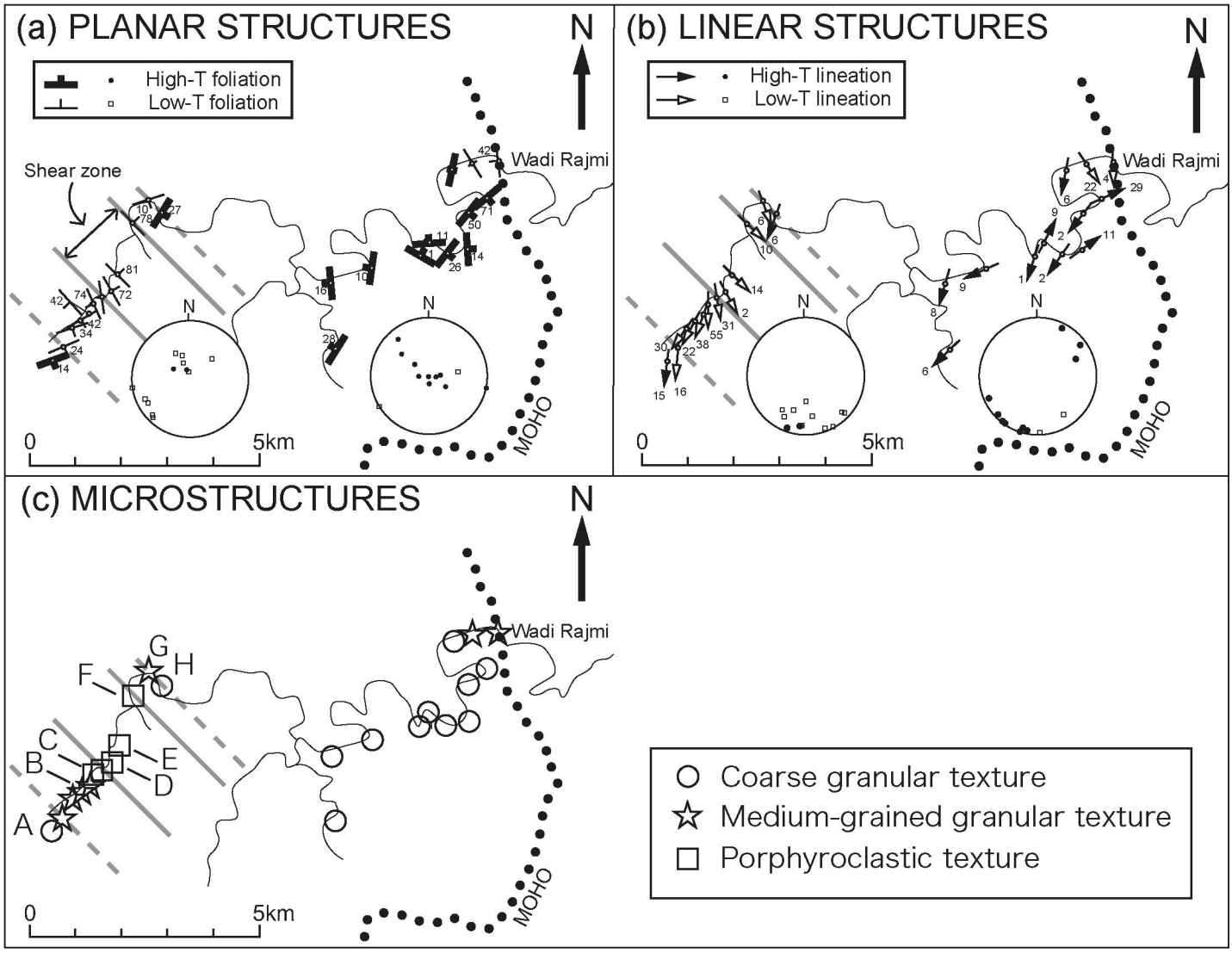

Fig. 2: Michibayashi, Ina and Kanagawa

Figure

Click here to download Figure: Fig 3-Microstructures300.eps

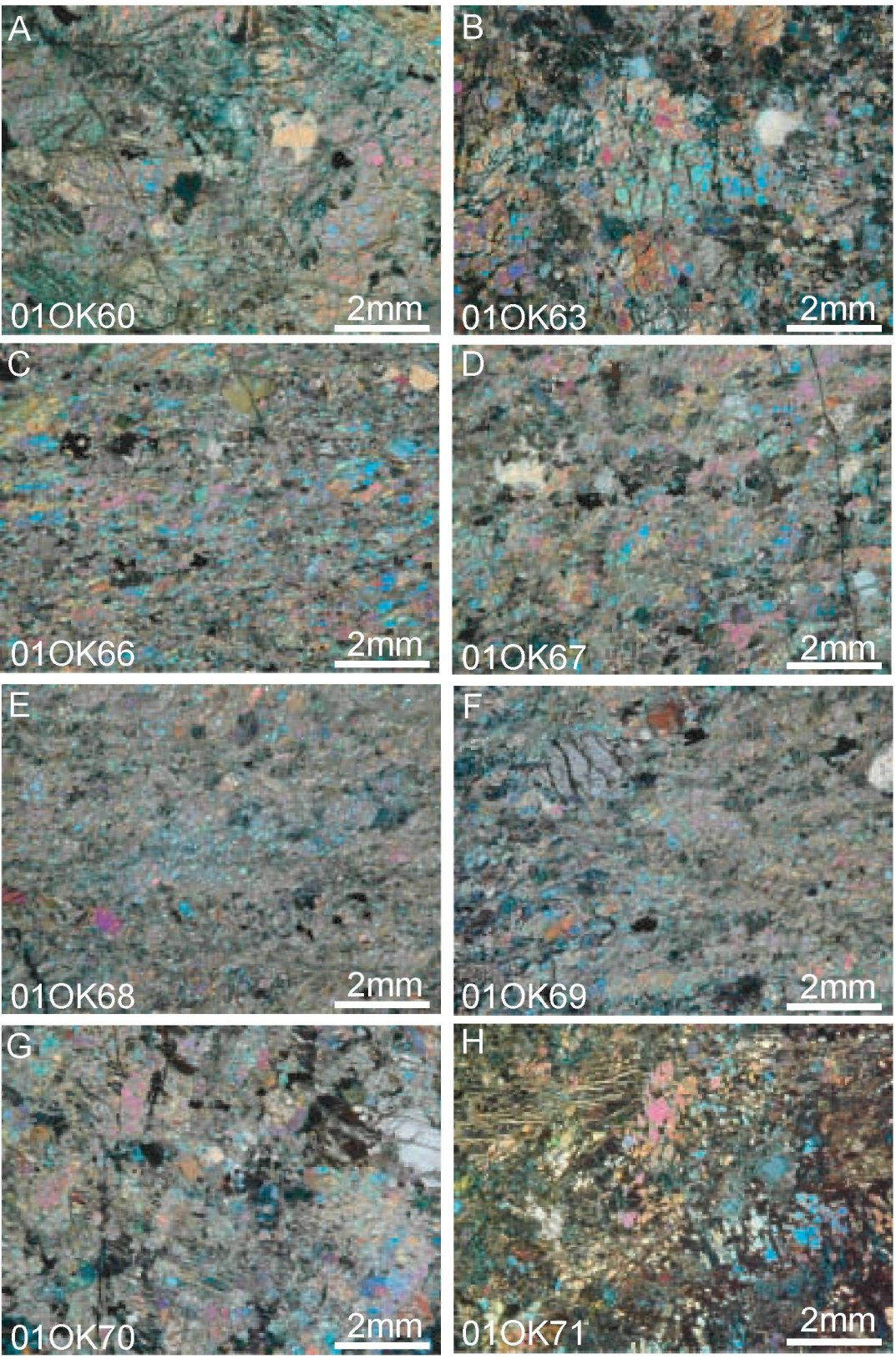

Figure 3: Michibayashi, Ina and Kanagawa

Figure
Click here to download Figure: Fig 4.eps

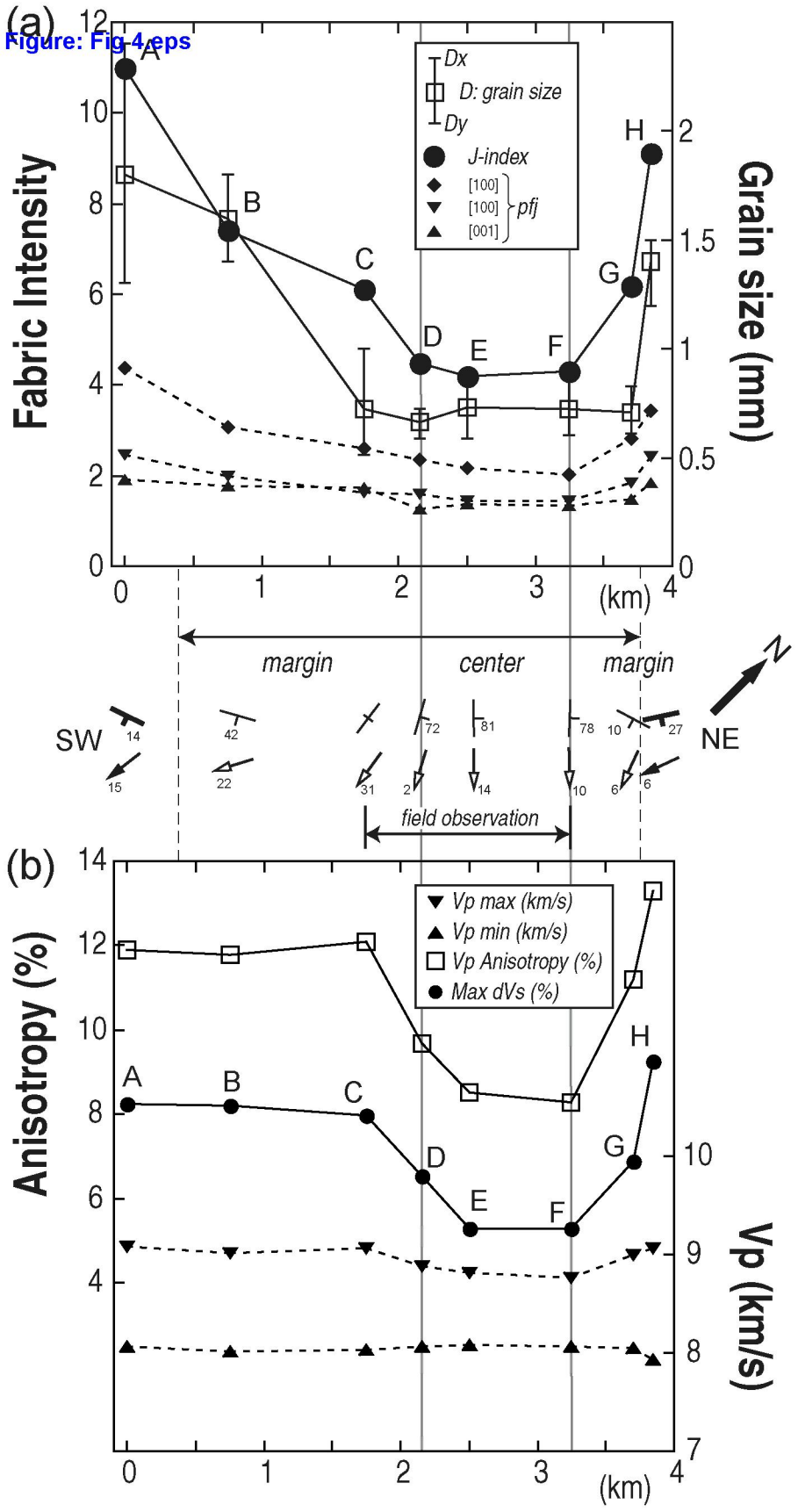

Figure 4: Michibayashi, Ina and Kanagawa

Figure

Click here to download Figure: Fig 5-CPO results.eps

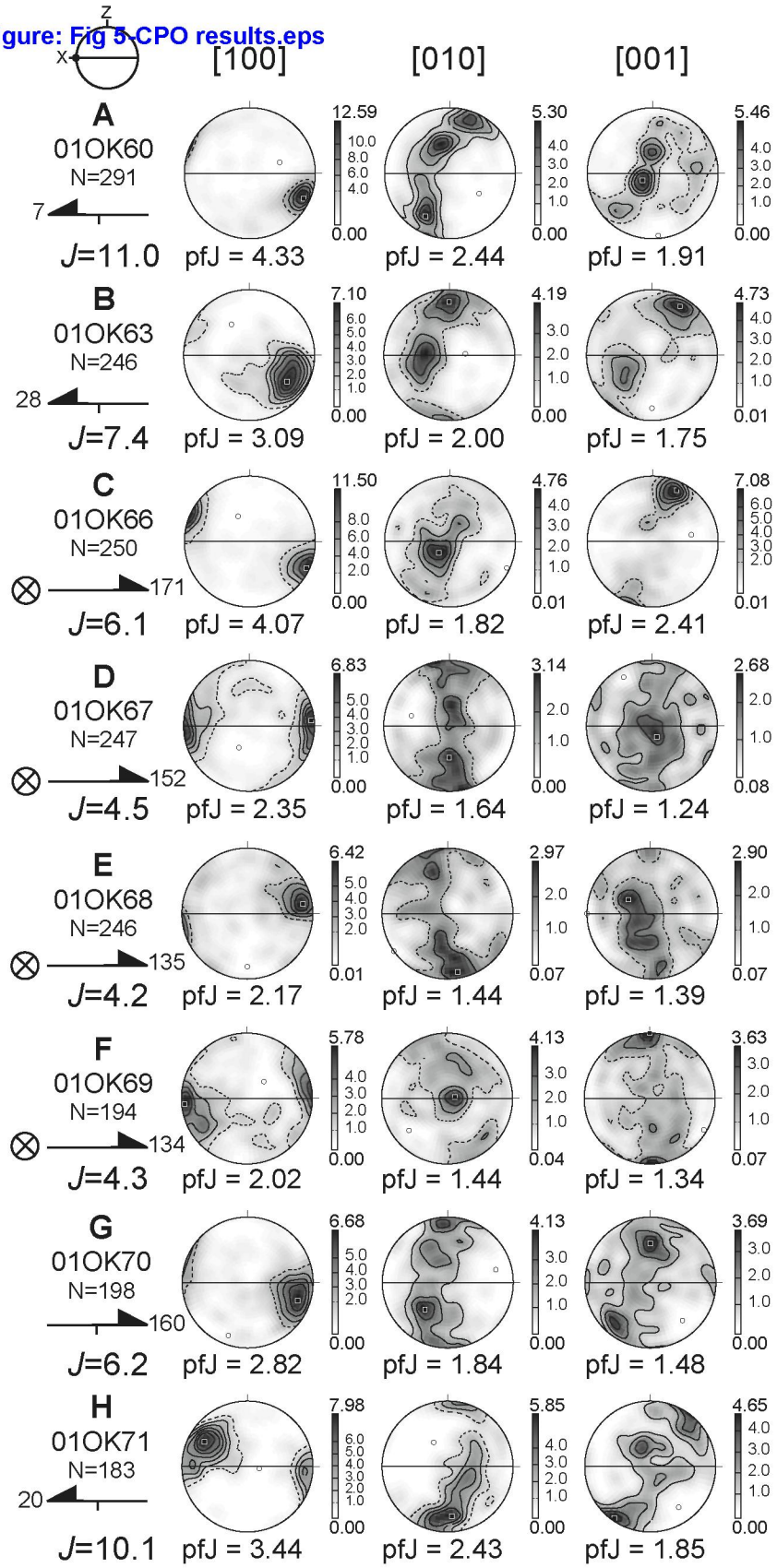

Fig. 5: Michibayashi, Ina and Kanagawa

Figure

Click here to download Figure: Fig 6-ANIS.eps

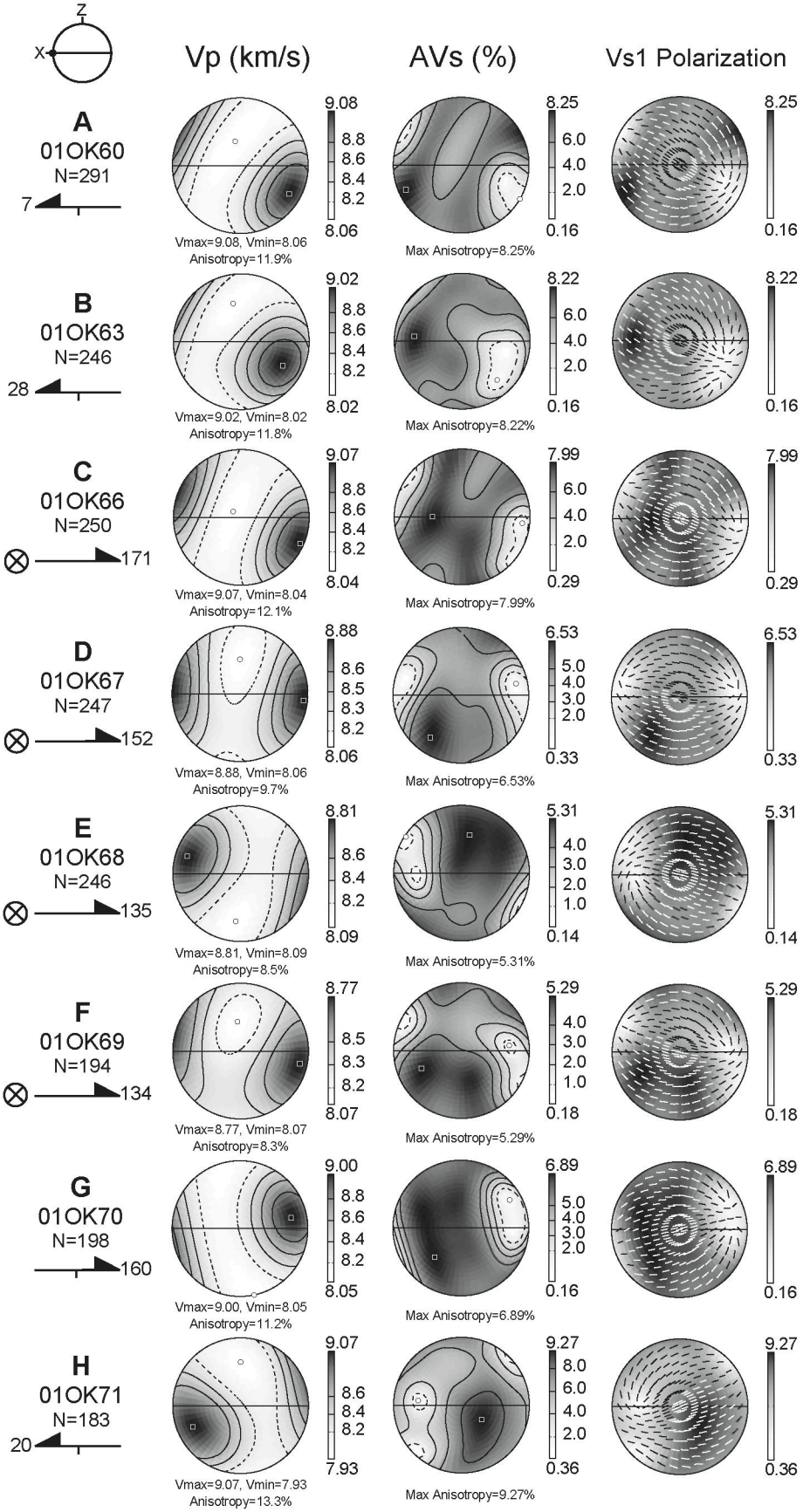

Figure 6: Michibayashi, Ina and Kanagawa

Figure

Click here to download Figure: Fig 7-paleopiezometer.eps

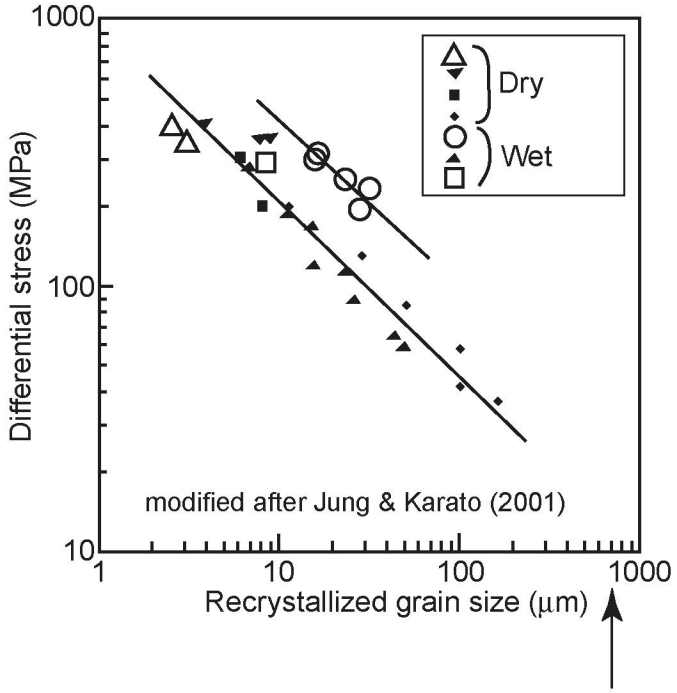

Fig. 7: Michibayashi, Ina and Kanagawa

Figure

Click here to download Figure: Fig 8-Anis vs J-index.eps

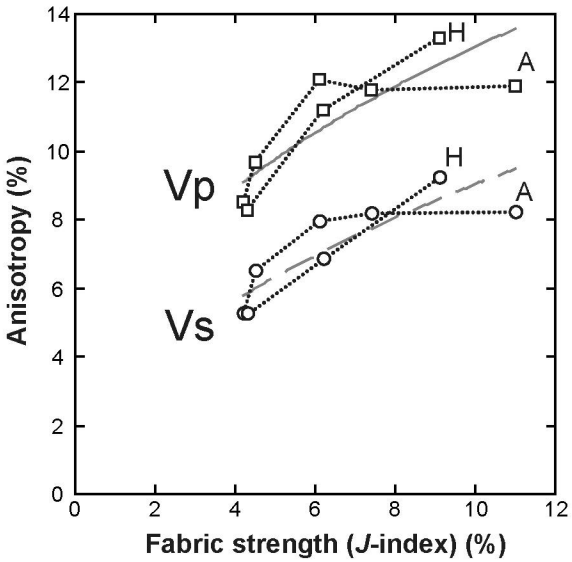

Figure 8: Michibayashi, Ina and Kanagawa

Table

Click here to download Table: Table 01.xls

Table 1: Michibayashi, Ina and Kanagawa

	Sample	Rock	Texture	Degree of recrystallization	Distance (km)	Grains for Dx	Grains for Dz	Dx (mm)	Dz (mm)	D (mm)	Grains for CPO
A	01OK60	hartzburgite	Coarse granular	no	0.00	43	44	2.40	1.30	1.80	280
B	01OK63	hartzburgite	Medium-grained granular	weak	0.75	78	79	1.80	1.40	1.60	248
C	01OK66	hartzburgite	Porphyroclastic	intense	1.75	101	117	1.00	0.51	0.72	274
D	01OK67	hartzburgite	Porphyroclastic	intense	2.15	98	96	0.72	0.59	0.66	249
E	01OK68	hartzburgite	Porphyroclastic	intense	2.50	103	105	0.89	0.59	0.73	246
F	01OK69	hartzburgite	Porphyroclastic	intense	3.25	100	107	0.87	0.60	0.72	194
G	01OK70	hartzburgite	Medium-grained granular	moderate	3.70	102	98	0.61	0.83	0.71	198
H	01OK71	hartzburgite	Coarse granular	no	3.85	65	64	1.50	1.20	1.40	183

Table

Click here to download Table: Table 02.xls

Table 2: Michibayashi, Ina and Kanagawa

No.	Sample	J-index	pfj			Vp			Vs1			Vs2			dVs
			[100]	[010]	[001]	Max (km/s)	Min (km/s)	Anisotropy (%)	Max (km/s)	Min (km/s)	Anisotropy (%)	Max (km/s)	Min (km/s)	Anisotropy (%)	Max (%)
A	01OK60	11.0	4.39	2.47	1.93	9.08	8.06	11.9	5.05	4.83	4.6	4.86	4.59	5.8	8.25
B	01OK63	7.4	3.07	1.99	1.76	9.02	8.02	11.8	5.04	4.87	3.5	4.89	4.57	6.7	8.22
C	01OK66	6.1	2.59	1.62	1.73	9.07	8.04	12.1	5.06	4.83	4.7	4.89	4.57	6.8	7.99
D	01OK67	4.5	2.35	1.61	1.25	8.88	8.06	9.7	5.00	4.85	3.1	4.87	4.64	4.9	6.53
E	01OK68	4.2	2.17	1.44	1.39	8.81	8.09	8.5	4.97	4.84	2.6	4.87	4.65	4.7	5.31
F	01OK69	4.3	2.02	1.44	1.34	8.77	8.07	8.3	4.99	4.83	3.2	4.87	4.66	4.4	5.29
G	01OK70	6.2	2.82	1.84	1.48	9.00	8.05	11.2	5.00	4.86	2.8	4.89	4.59	6.4	6.89
H	01OK71	9.1	3.44	2.43	1.85	9.07	7.93	13.3	5.03	4.82	4.4	4.92	4.55	7.8	9.27